AIAA JOURNAL
Vol. 36, No. 11, November 1998

Unsteady Crossflow Separation Location Measurements on a Maneuvering 6:1 Prolate Spheroid

Todd G. Wetzel* and Roger L. Simpson†
Virginia Polytechnic Institute and State University, Blacksburg, Virginia 24061-0203

The crossflow separation of a 6:1 prolate spheroid undergoing transient maneuvers is studied. The dynamic plunge–pitch–roll model mount provides the unique capability to simulate unsteady maneuvers in a wind tunnel. Hot-film sensors are used with constant-temperature anemometers to measure the time-dependent wall shear at points over the entire model surface. Minima in wall shear are used to indicate separation locations. Steady and unsteady data are presented for two fast maneuvers: a 0–30-deg, 0.33-s ($t' = tU_\infty/L = 11$) ramp pitchup about the model center (pitchup maneuver) and a 0–13.5-deg, 0.25-s ($t' = 8.3$) pitchup about the model center that simulates the time-dependent sideslip angle of a submarine entering a turning maneuver (submarine maneuver). Data show that, especially at higher angles of attack, significant lags occur in the flowfield during the maneuvers compared with the steady cases. In particular, separation is delayed at all locations of the model by up to a 10-deg higher angle of attack in the unsteady maneuvers compared with the steady data. Equivalently, the separation structure during the unsteady maneuvers lags the steady data by from 1.5 to 3.5 nondimensional time units t'. A first-order lag model fits the unsteady separation data, and the resulting time lags indicate that disturbances are propagated at speeds slower than freestream due to slower convective speeds of the boundary layer.

Nomenclature

C_f	= skin-friction coefficient, τ_ω/q_∞
$\boldsymbol{F}$	= generalized steady and quasisteady aerodynamic vector function
$\boldsymbol{G}$	= generalized unsteady aerodynamic vector function
$\bar{h}$	= heat transfer film coefficient
L	= model length
q_∞	= dynamic pressure, $\frac{1}{2}\rho U_\infty^2$
Re_D	= diameter-based Reynolds number, $U_\infty D/\nu$
Re_L	= length-based Reynolds number, $U_\infty L/\nu$
t	= time
t'	= nondimensional time, tU_∞/L
U_c	= unsteady convection velocity
U_τ	= friction velocity, $U_\infty(Cf/2)^{1/2}$
U_∞	= freestream velocity
x	= model longitudinal position from nose
x_{cg}	= location of center of rotation
y	= wall normal coordinate
y^+	= $y\rho U_\tau/\mu$
z	= dynamic plunge–pitch–roll (DyPPiR) plunge ordinate
α	= DyPPiR pitch angle and model center angle of attack
α_{eff}	= effective angle of attack, $\alpha - \Delta\alpha_{\text{eff}}$
$\dot{\alpha}$	= dimensional pitch rate
$\bar{\dot{\alpha}}$	= nondimensional pitch rate, $\dot{\alpha}L/U_\infty$
β	= sideslip angle
$\Delta\alpha_{\text{eff}}$	= incremental effective angle of attack; Eq. (2)
μ	= viscosity
ρ	= air density
τ_ω	= wall shear stress
τ'	= first-order time lag in nondimensional time units
ϕ	= circumferential location on model surface
ϕ_{sep}	= separation location

Received April 19, 1997; revision received July 24, 1998; accepted for publication July 29, 1998.

*Research Associate, Aerospace and Engineering Department; currently Engineer, Heat Transfer, General Electric Corporate R&D Center, Schenectady, NY 12301. Member AIAA.

†Jack E. Cowling Professor, Aerospace and Ocean Engineering Department. Fellow AIAA.

I. Introduction

A. Unsteady Aerodynamics

With recent efforts to expand submarine, aircraft, and ordinance dynamic performance beyond conventional regimes, the need for studying truly unsteady, high-excursion, high-Reynolds-number flows has increased. Standard stability derivation techniques fail to capture the nonlinearities in such flows, and computational fluid dynamics techniques cannot accurately compute the highly complex, separated flowfields of full vehicle geometries in steady conditions, let alone unsteady ones. Such methods are deficient only because they lack physical models on which to base their computations that accurately describe the complexities of a time-dependent, turbulent, separated flowfield. These models can be developed only with suitable experimental flowfield data from sufficiently realistic flows. A new apparatus in the Stability Wind Tunnel at Virginia Polytechnic Institute and State University, the dynamic plunge–pitch–roll (DyPPiR) model mount (Fig. 1), provides for the first time the capability to simulate truly time-dependent, high-excursion, high-Reynolds-number flows in a laboratory setting.[1,2]

Dynamic testing has been an important part of design and validation of various types of craft for decades. Typically, these techniques have been relying on very small-amplitude sinusoidal oscillations that can describe small-excursion maneuvers reasonably well.[3] Even in these tests, however, the measurements are usually limited to forces and moments. Seldom are flowfield data taken in dynamic tests.

It is important to clearly identify the distinction between quasisteady and unsteady aerodynamics. Quasisteady describes any technique or analysis that assumes that the aerodynamics of a maneuvering body are dependent only on the instantaneous state of the model (α, β, control surface deflections, etc.) and, therefore, requires sufficiently small rate-dependent parameters, e.g., $\dot{\alpha}$, $\dot{\beta}$, etc. Fully general unsteady aerodynamics, unlike quasisteady techniques, includes explicit time dependency, or history effects, of the aerodynamics. Mathematically, this distinction can be summarized as follows, where the time is nondimensionalized by the time for flow to pass over a model L/U_∞, or $t' = tU_\infty/L$ (Ref. 4): steady, $\boldsymbol{F}(\alpha, \beta, \ldots)$; quasisteady, $\boldsymbol{F}[\alpha(t'), \beta(t'), \ldots]$; and fully unsteady, $\boldsymbol{G}[t', \alpha(t'), \beta(t'), \dot{\alpha}(t'), \dot{\beta}(t'), \ldots]$.

B. 6:1 Prolate Spheroid

The prolate spheroid is an interesting geometry because the flowfield is very complicated even though the body shape is very simple. In addition, the prolate spheroid flowfield is qualitatively

Table 1 Comparative Reynolds numbers and nondimensional pitch rates from unsteady body aerodynamic experiments

Authors	Model	Wind or water tunnel	Re_L	$\bar{\dot{\alpha}} = \dot{\alpha}(L/U_\infty)$	α range, deg	Measurements
Gad-el-Hak and Ho[6]	Ogive cylinder	Water	4×10^4	1.05	0–30	Flow visualization
Montividas et al.[7]	Cone cylinder	Wind	5.665×10^4	0.7	0–90	Flow visualization, some wake LDV
Smith and Nunn[8]	Ogive cylinder	Wind	1.2×10^6	0.0405	−15–105	Flow visualization forces and moments
Panzer et al.[9]	Hemisphere cylinder	Wind	2.29×10^5	0.0065	15–30	Wake LDV
Panzer et al.[9]	Hemisphere cylinder	Water	7.5×10^4	0.1	15–30	Wake LDV
Brandon and Shah[10]	F-18	Wind	1.6×10^6	0.0364	−10–80	Flow visualization forces and moments
Present work	6:1 prolate spheroid	Wind	4.2×10^6	0.047	0–30	Hot film

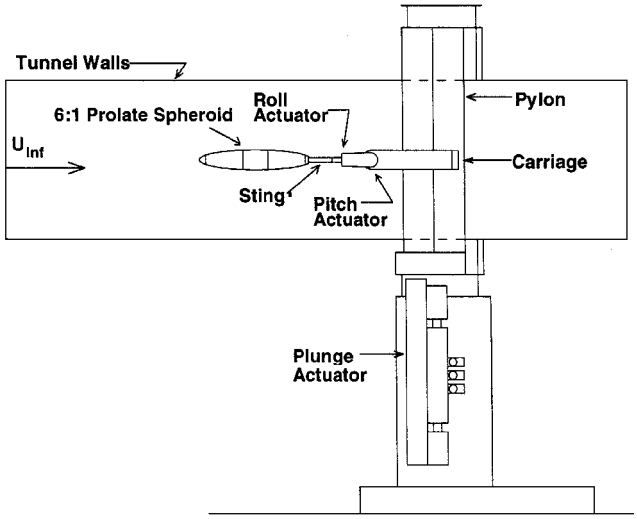

Fig. 1 DyPPiR model mount installed in wind tunnel.

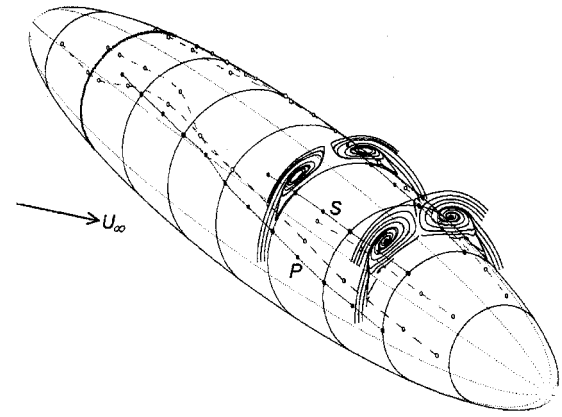

Fig. 2 Crossflow separation topology. Minima in skin friction (– – –) indicate separation locations, and oil flows (—) indicate separation location biased windward[15]; LDV and hot-wire anemometer data from Ref. 17 show vortical separation; α = 20 deg, $Re_L = 4.2 \times 10^6$.

similar to that of submarines, missiles, torpedoes, and to a certain extent aircraft fuselages. Wetzel[5] gives a brief overview of the well-documented steady prolate spheroid literature along with a detailed description of the steady flowfield. The prolate spheroid flowfield at angle of attack is characterized by crossflow separation that forms on the tail at low angles of attack and migrates windward and noseward at increasing angles of attack[5] (Fig. 2). The circumferential location of separation and even the separation topology are highly dependent on the state of the local boundary layer, that is, whether it is laminar, transitional, or turbulent.

All models tested were 1.372-m-long 6:1 prolate spheroids with circular cross section. The maximum radius was 114 mm. The rearmost 38 mm was removed to allow for sting entry. In all runs, the tunnel speed was set to 45.7 m/s, yielding a Reynolds number based on length of 4.2×10^6, which is well above the established critical Reynolds number of 2.5×10^6 (Ref. 2). This critical Reynolds number is fully valid up to 20-deg angle of attack. Above $\alpha = 20$ deg, there seems to be a small Reynolds number effect, evidenced by a difference between tripped and untripped force and moment data. This difference is probably due to the influence of laminar separation on the nose. In all cases, trip posts were placed at $x/L = 0.20$ to fix transition and further guarantee a Reynolds-number-insensitive separation over the rear 80% of the model at angles of attack in excess of 20 deg. The trip posts were 0.53-mm-high cylinders, 1.3 mm in diameter and spaced 2.5 mm apart. Upstream of the trips, at high angles of attack, the laminar flow will separate, undergo transition, reattach, and reseparate as a second, turbulent separation. These two separation lines merge downstream of the trip posts.[5]

C. Previous Studies

Few experiments in unsteady aerodynamics have focused on three-dimensional turbulent, separated flow. In steady aerodynamics, turbulent three-dimensional separations involve very distinct mechanisms compared with laminar and/or two-dimensional flows. It is then assumed that, in unsteady aerodynamics, a complication of steady aerodynamics, turbulent three-dimensional separations bear no resemblance to two-dimensional or laminar counterparts; thus, such studies are irrelevant and not reviewed here. Table 1 lists the few relevant, three-dimensional, unsteady aerodynamic experiments[6–10] conducted on various bodies and their comparative Reynolds numbers (most of which are indeed laminar), nondimensional pitch rates, and types of measurements. It has been established that, in steady flows over a prolate spheroid with no boundary-layer tripping, crossflow separation is insensitive to Reynolds number above a critical Re_L of 2.5×10^6 (Ref. 2). Note that the present work has the highest Reynolds number and in fact is the only test with a Reynolds number in excess of the critical Reynolds number of 2.5×10^6. The current tests also have a moderate pitch rate and angle-of-attack range compared to previous work. It is believed that such a pitch rate will not significantly affect the critical Reynolds number. Also, the trip strips help to guarantee that there is no change in critical Reynolds number at high angles of attack. Therefore, including the trip strips, the current work is the one least likely to have Reynolds number effects. Also, this is the first work to implement fine-spatial-resolution surface hot-film measurements on a maneuvering body. Most of the other experiments focus on flow features other than separation, such as vortex location and breakdown. Their general observations about the effects of unsteadiness on the flow are compared with the observations in this work, though these observations may be about different phenomena.

D. Objectives of Current Work

The current work fills many voids in the literature. The maneuvers studied here are large-excursion maneuvers as opposed to small-perturbation maneuvers. The goal is to detect the time history of the formation and migration of the crossflow separation that forms during such a maneuver. Section II describes the hardware used in the experiments and the maneuvers tested. Section III presents both steady and unsteady hot-film data. Finally, Sec. IV includes a discussion of the results in terms of the fluid dynamics responsible for the unsteady effects.

II. Instrumentation and Experimental Techniques

A. Wind Tunnel and DyPPiR Model Mount

The DyPPiR is installed in the Virginia Polytechnic Institute 1.8 × 1.8 m Stability Wind Tunnel (Fig. 1). The stability tunnel is a closed-return, closed test session, subsonic facility with a maximum speed of over 80 m/s. Turning vanes, screens, and a 9:1 contraction ratio inlet nozzle reduce the freestream turbulence to about 0.03% (Ref. 11). The fan is powered by a 450-kW dc motor. For these tests, the tunnel speed was held constant at 45.7 m/s (within ±1%). Because the tunnel temperature is ambient, the Reynolds number varied by ±5% over the course of the experiments.

The DyPPiR combined three 20.6-MPa hydraulic actuators to plunge a model through a 1.5-m range vertically, pitch the model through a ±45-deg range, and roll the model through a ±140-deg range. The three actuators provide the power required to force 45 kg of model and over 250 kg of DyPPiR hardware at rates approaching 9 m/s in a plunge and over 90 deg/s in pitch. Most importantly, however, the DyPPiR is digitally controlled by a personal computer, so that it is capable of performing general, preprogrammed maneuvers. It is not limited to sinusoids or fixed rate ramps. The nomenclature used for the three degrees of freedom, along with body nomenclature, is shown in Fig. 3. Typically models are up to 2 m long, and typical maneuvers last several tenths of a second. Even at Reynolds numbers of over 4×10^6, the maneuvers are fast enough to exhibit significant unsteadiness. Thus, the DyPPiR successfully fills the need of forcing a model to perform general, rapid, truly unsteady, high-excursion, high-Reynolds-number maneuvers.

Most parameters studied are related to the instantaneous angle of attack. The DyPPiR specifically sets a pitch actuator position during a maneuver. Because for all of the maneuvers studied the model is pitched about the model center, it can be stated that the DyPPiR pitch angle is equal to the instantaneous angle of attack of the model, referenced at the model center. Because of the motion of the model, the instantaneous local angle of attack varies linearly from the nose to the tail of the model, with the nose being at a lower angle of attack than the model center and the tail at a higher angle of attack than the model center. The magnitude of the local induced increment in angle of attack is a function of distance from the model center and rotational speed. In all cases studied, these angle-of-attack increments, relative to the model center angle of attack, are less than 1.4 deg at the extreme nose and tail. Also, recent tests have confirmed that the sting mount places the model far enough from the main DyPPiR strut to make strut interference negligible.[12]

B. DyPPiR Maneuvers of the Prolate Spheroid

The pitchup maneuver is a simple linear ramp from 0 to 30 deg in 0.33 s. No specific acceleration or deceleration curves were programmed. The objective is to get as abrupt a start and stop as possible. The DyPPiR does, in any case, have a finite acceleration and deceleration capability. Figure 4 shows actual pitch angle position feedback taken during several hundred maneuver executions. The solid line is the mean over the ensemble, and the dotted lines delineate two-standard-deviation(2σ) boundaries. The model is pitched about the model center, so that the carriage is plunged roughly 70 cm during the maneuver to prevent the model center from moving vertically. Figure 5 shows the plunge position feedback data for the same maneuver. Although it is possible to keep the model center from moving vertically during a maneuver, it is inevitable that the model center will translate downstream during a maneuver. This downstream movement amounts to roughly 1% of the freestream velocity and is, thus, deemed insignificant.

The submarine maneuver is modeled after data for a full-scale submarine during the initial transient portion of a turning maneuver. For the DyPPiR tests, the submarine maneuver models the time history of the sideslip angle from the actual submarine tests (Fig. 6). This is characterized by a ramp up to 13.5 deg with a slight overshoot. Also, the motion simulated on the DyPPiR is roughly half the nondimensional speed of full scale.

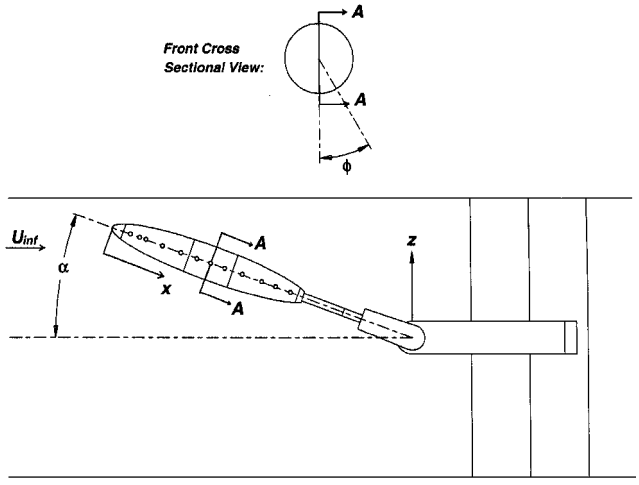

Fig. 3 Coordinate nomenclature: x is measured from the nose, ϕ is the circumferential location measured from the windward line of symmetry, z is the plunge ordinate, and α is the pitch angle.

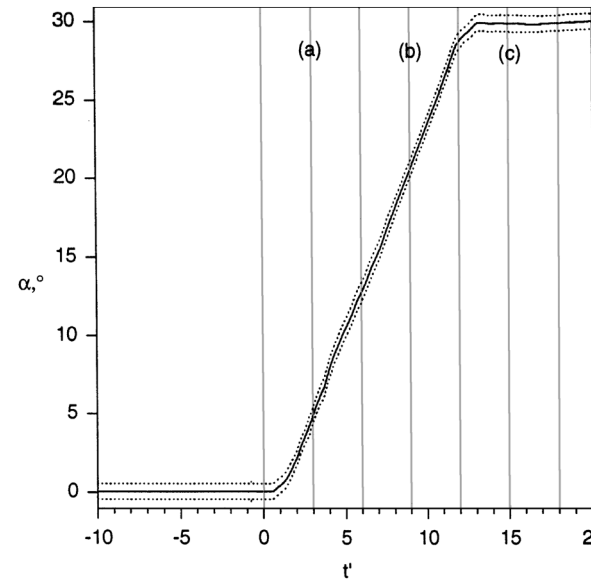

Fig. 4 Pitch-up maneuver pitch angle position feedback. Dotted lines represent 20:1 odds positional repeatability.

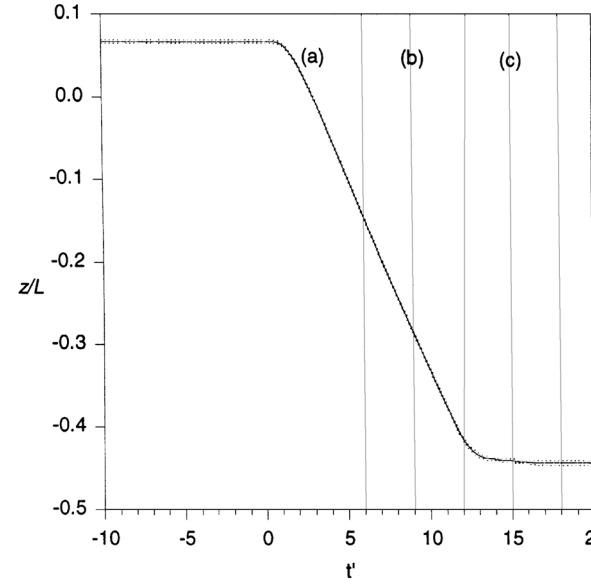

Fig. 5 Pitch-up maneuver plunge position feedback. Dotted lines represent 20:1 odds positional repeatability.

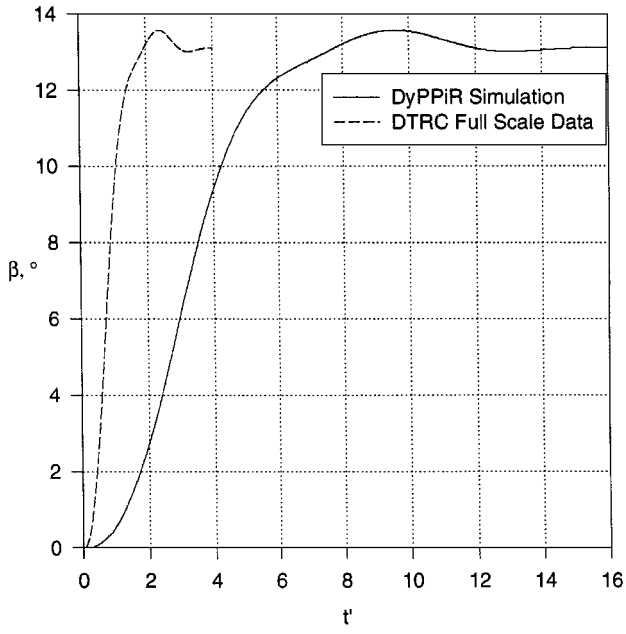

Fig. 6 Submarine maneuver pitch angle command signal compared to data from David Taylor Model Basin sideslip data.

C. Hot-Film Measurements

The surface skin friction was measured with the hot-film sensors designed and documented by Simpson et al.[13] The sensors were operated with constant-temperature anemometers, and the sensor/anemometer system had a flat frequency response out to roughly 200 Hz. A detailed description of the sensors, their application to the model, and the instrumentation used to operate the sensors can be found in Ref. 5. The sensors heat the near-wall fluid through forced convection. Because of the similarity between gradient transport of momentum and scalars (heat), the heat transfer in the fluid gives a measure of the wall shear. The mean film coefficient $\bar{h}$ is proportional to the cube root of the near-wall velocity gradient, which is thus proportional to the wall shear.[13,14] The main purpose of the sensors is not necessarily to measure the absolute magnitude of the wall shear or the skin-friction coefficient but to measure the relative shear distributions through measurements of the film coefficient to locate shear minima and, thus, separation locations. However, wall shear magnitudes are possible with adequate calibration.

Wetzel et al.[15] establish that wall shear magnitude minima are one of the simplest and most accurate indicators of three-dimensional crossflow separation. This is primarily due to the presence of a low-velocity trough that occurs at crossflow separations and results in a small skin-friction magnitude.

For a detailed description of the apparatus and uncertainties, see Ref. 5. The custom-designed, directionally insensitive surface hot-film sensors were mounted at 12 locations along a lengthwise surface element: $x/L = 0.118$, 0.194, 0.220, 0.271, 0.347, 0.424, 0.500, 0.576, 0.653, 0.729, 0.831, and 0.882. The sensors were each connected to nonlinearized Miller-type, constant-temperature anemometers.[16] The DyPPiR roll actuator was used to position this strip at specific circumferential locations from $\phi = 0$ to 180 deg to map the circumferential skin-friction distributions in increments of 5 deg on the windward side and 2 deg on the leeward side. A data acquisition board in a personal computer was used to read the sensor voltages. Tunnel temperature, total pressure, and dynamic pressure were all measured as well, as were DyPPiR positional outputs. For each ϕ model orientation, a given maneuver was executed 10 times. Squared voltages for a given sensor at a given roll orientation and a given point in time were averaged over the 10 ensembles. Further details of the data reduction procedure can be found in Ref. 5.

The relative uncertainty between two measurements made by a given sensor and, thus, the relative uncertainty between any two measurements presented in a given circumferential distribution is ±5% for combined random and bias uncertainties at 20:1 odds. Because of calibration uncertainties, the uncertainty between any measurements made by two different sensors (and thus at two different axial model stations) is ±20%. The latter uncertainty is unimportant, however, because circumferential distributions of skin friction are used to determine separation locations and are, thus, governed by the former ±5% uncertainty. Because of low-frequency response and large sensor size (5 mm), the sensors are insensitive to high-frequency, small-scale, turbulent fluctuations. The frequency response is high enough (200 Hz) for the sensors to accurately track temporal changes in the spatially averaged skin-friction values.

III. Results

A. Steady Results

Figure 7 shows the constant-temperature, hot-film anemometer skin-friction coefficients superimposed on top of secondary streamlines determined by Chesnakas and Simpson[17] from detailed laser Doppler anemometer velocity measurements. Note that the skin-friction values are not to scale, but the streamline plots are. In fact, the secondary streamline plots represent data taken up to approximately 3 cm away from the wall and, thus, represent the near-wall flowfield in these separated zones. The radial grid lines represent locations where the laser Doppler velocimetry (LDV) data were actually taken; therefore, separation uncertainties in this data set are limited by the 5-deg spacing of the profile locations. Each profile contains 17 points spaced logarithmically down to 0.007 cm from the wall, corresponding to y^+ values on the order of 7. In all cases, the wall shear minimum qualitatively corresponds to the separation location but seems to exhibit a positional lag. The apparent separation location indicated by these secondary streamlines is essentially a reflection of the location where the circumferential velocity component is zero. Because a separation line is a streamline, the real separation line occurs where the local velocity perpendicular to it is, of course, zero, and because a separation line is in general not parallel to the body axis, this is a different location from where the circumferential velocity is zero. This subtlety is discussed in detail in Ref. 15, where it is shown that, by representing the velocity data in a coordinate system that is parallel to the separation line direction and not parallel to the body axis, the true separation line thus indicated by the LDV data corresponds exactly, within the uncertainties, to the minima in skin friction. Therefore, for the remainder of this paper, skin-friction minima are assumed to indicate separation location.

Figure 8 shows circumferential skin-friction distributions over the length of the model for $\alpha = 15.2$ deg. At the rearmost sensor ($x/L = 0.882$), two minima are seen, indicating a primary and secondary separation. The secondary separation extends only up to

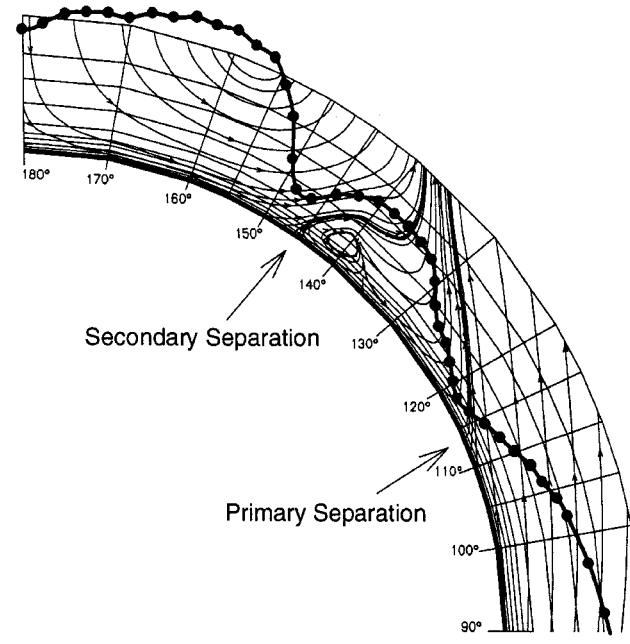

Fig. 7 Steady flow skin-friction values superimposed on secondary streamlines from Ref. 17 at $x/L = 0.77$ and $\alpha = 20$ deg.

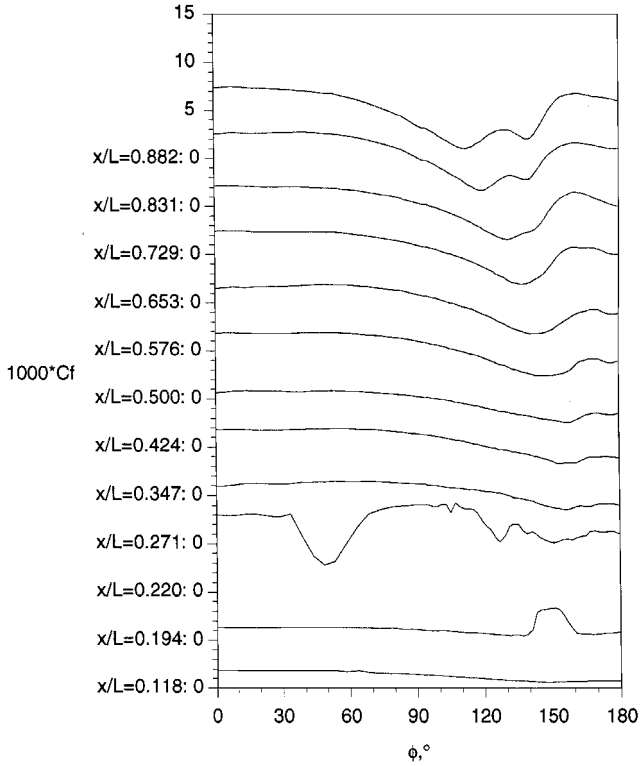

Fig. 8 Steady flow C_f vs ϕ for all x/L, α = 15.2 deg.

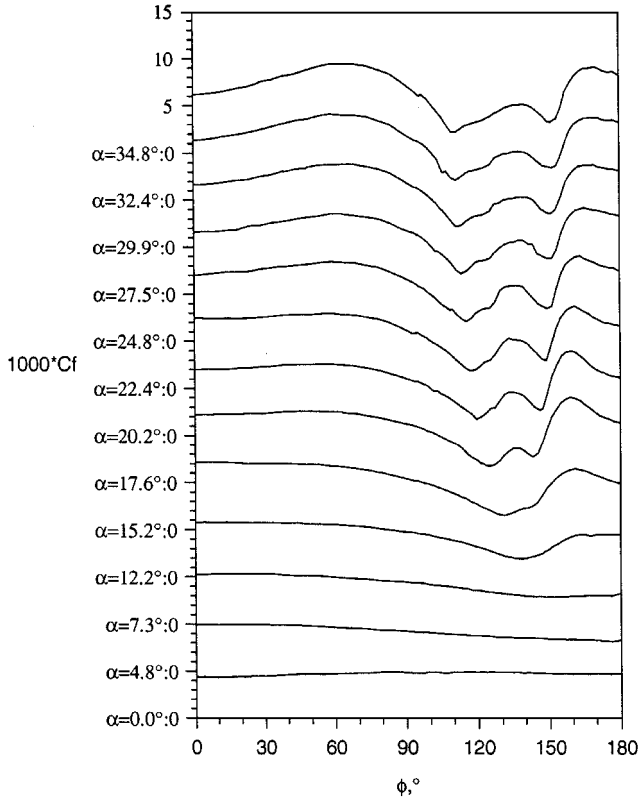

Fig. 9 Steady flow C_f vs ϕ for all α, x/L = 0.729.

$x/L = 0.729$. Upstream, the primary separation minima are located farther leeward and are weaker. The distribution at $x/L = 0.220$ is very irregular because this sensor was immediately downstream of the trip posts, where the flow had not completed transition to turbulence.

Figure 9 shows how the circumferential skin-friction distributions at one location ($x/L = 0.729$) vary with angle of attack. At this location, a minimum indicating primary separation is first evident at

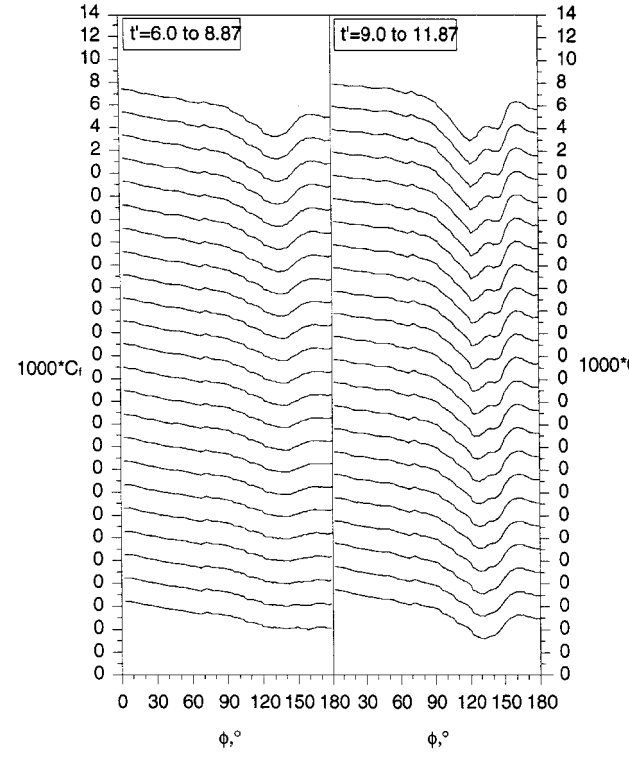

Fig. 10 Pitchup maneuver time development of C_f vs ϕ for x/L = 0.729; times in columns correspond to time period b in Figs. 4 and 5.

$\alpha = 12.2$ deg. This minimum grows in strength and moves windward as the angle of attack increases. A second minimum, indicating secondary separation, is fully developed by $\alpha = 17.6$ deg. It, too, grows in strength at increasing angle of attack but remains in roughly the same circumferential location.

The locus of the minima in these distributions for each axial station describes the separation topology (for example, see the dashed-line/open symbols of Fig. 2). At this angle of attack (20 deg), two separations are evident on the nose due to a laminar separation that undergoes transition, reattaches, and reseparates as a turbulent separation. Also, a strong secondary separation extends over the rear 40% of the model length.

B. Unsteady Results

Figure 10 shows the circumferential skin-friction distributions for $x/L = 0.729$ at discrete time steps during the pitchup maneuver. Time increases from bottom to top in these plots, and the range of time encompassed by a given plot column is indicated at the top of each column. The flow is essentially attached at the first time step ($t' = 6.0$), but a primary separation is formed by the top of the first column ($t' = 8.87$). Similarly, a secondary separation is formed by the top of the second column in Fig. 10 ($t' = 11.87$).

The wall shear minimum can be located for each time step to generate a plot of the separation location vs time. Figure 11 shows an example of such a plot for $x/L = 0.729$. The steady separation locations for the instantaneous angles of attack are also plotted as a comparison. The primary separations lag the steady data significantly, by as much as 1.5–4.5 t' units.

Figure 12 shows a comparison of separation lines at $\alpha = 20$ deg for both the pitchup maneuver and the steady data. It is clear that the primary separation line in the pitchup maneuver lags the steady separation line by as much as 10 deg in the circumferential position, and where the steady data show a strong, well-developed secondary separation line, no such secondary line exists in the unsteady data.

Figure 13 shows the time history of the separation location (again, using wall shear minima) at $x/L = 0.729$ for the submarine maneuver. Note that the position feedback in Fig. 13 indicates the actual maneuver achieved given the input described by Fig. 6. The submarine maneuver involves a lower angle-of-attack range, and so there are only two steady data points with which to compare. Still, there

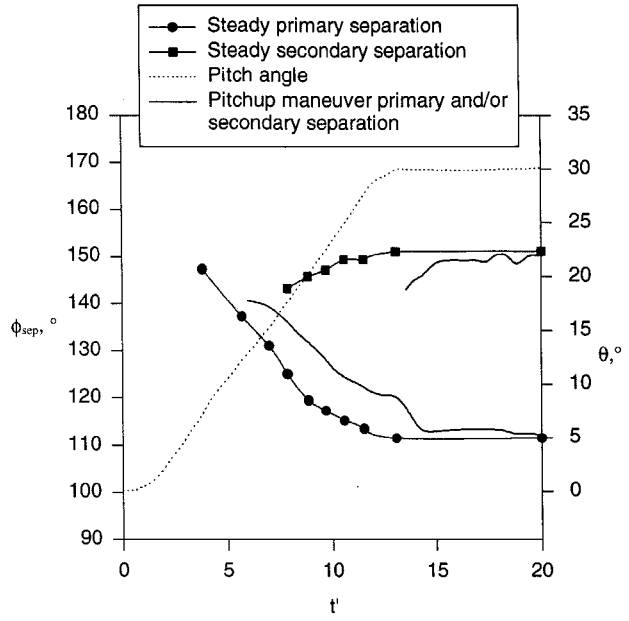

Fig. 11 Separation position vs time for pitchup maneuver at x/L = 0.729 compared with steady separation positions for instantaneous angles of attack α.

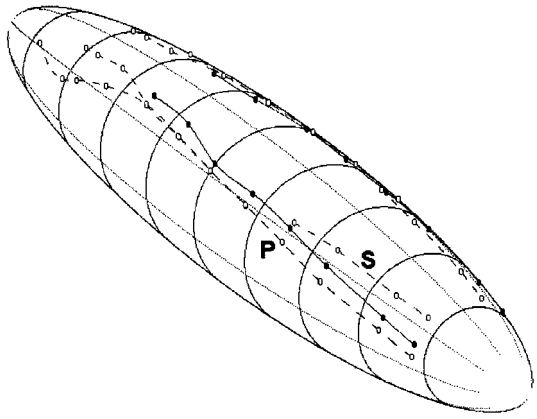

Fig. 12 Comparison of steady and unsteady (pitchup maneuver) separation lines at α = 20.2 deg (t' = 8.86): dashed lines/open symbols are equivalent steady separation lines, solid lines/closed symbols are separation lines from ensemble-averaged unsteady data at t' = 8.86, P indicates primary separation, and S indicates secondary separation.

is an evident lag in the separation formation even for this maneuver. Note that, from $t' = 7$ and onward, the differences between steady and unsteady are less than the uncertainties of the separation location measurement.[5]

Figures 14 and 15 show direct comparisons between steady circumferential skin-friction distributions and unsteady ones for $x/L = 0.729$. Figure 14 shows data for both the pitchup and submarine maneuvers compared with steady data at an angle of attack of 12.2 deg. In the steady data, a clear primary separation exists at $\phi = 135$ deg, but no separation is seen in either the pitchup or submarine maneuver at the instant the model reaches this angle of attack. In Fig. 14, the data from the last recorded time taken during the submarine maneuver, which occurs $t' = 20$ after the model has come to rest, show that the flow has essentially regained a steady-state condition. Note that this final position is actually at $\alpha = 13.6$ deg, slightly higher than the 12.2 deg of the other data curves in Fig. 14.

Figure 15 shows a comparison of the pitchup maneuver at 20-deg angle of attack with equivalent steady data. In this case, the steady data show both a primary and secondary separation, whereas the unsteady distribution shows only a primary separation that is weaker and more leeward than the steady primary separation. This shows that in unsteady flows the separation topology can be different from that in an equivalent steady configuration.

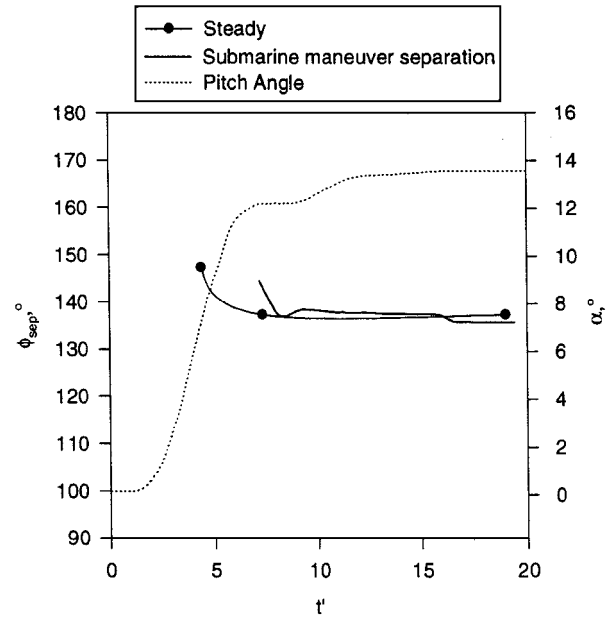

Fig. 13 Separation position ϕ_{sep} vs t' for submarine maneuver at x/L = 0.729 compared with steady separation positions for the same angle of attack α.

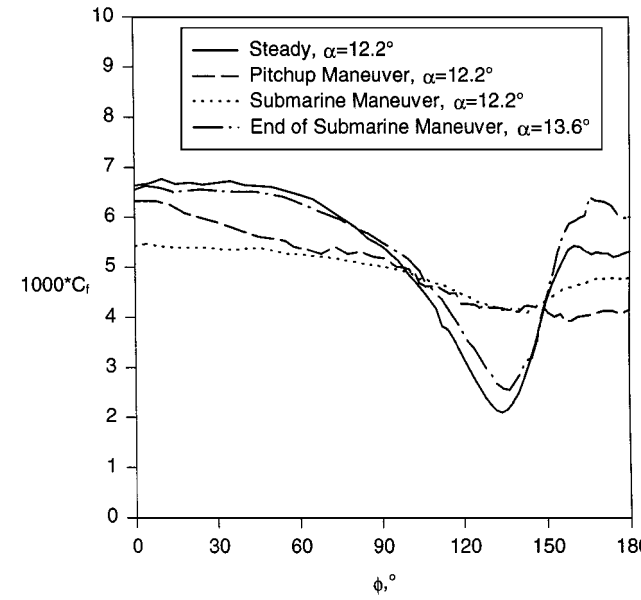

Fig. 14 Comparison of wall shear distribution at x/L = 0.729 for steady data, pitchup maneuver, and submarine maneuver at α = 12.2 deg.

IV. Discussion

A. Algebraic Time Lag Models

The data conclusively demonstrate that the unsteady separation formation lags the steady case. To understand why a lag exists, one can examine the path of a fluid particle during the maneuver, which will of course be different from the path of a similar particle in a steady flowfield. A fluid particle immediately at separation during the pitchup maneuver began its trajectory on the windward side of the model when the model was at a lower angle of attack. Therefore, the particle has experienced a less severe adverse pressure gradient along its pathline and, as a result, can travel farther around the leeside of the model before separating when compared with a similar particle in a purely steady flowfield. It is this history effect, an effect dependent on the true total path the particle has traversed, that differentiates the unsteady flowfield from the steady one.

The lag in separation formation means that, at any instantaneous angle of attack, the separation starts farther back from the nose and more leeward in the unsteady case compared with the steady case. The total separated region occupies a smaller area, both on

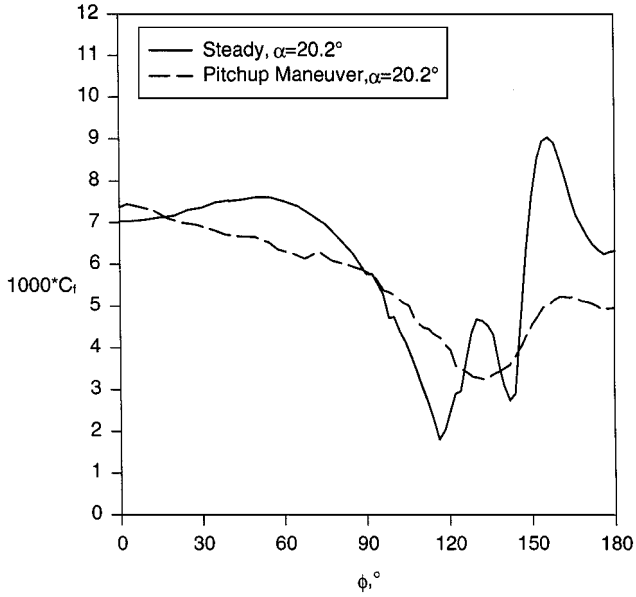

Fig. 15 Comparison of wall shear distribution at $x/L = 0.729$ for steady data and pitchup maneuver at $\alpha = 20.2$ deg.

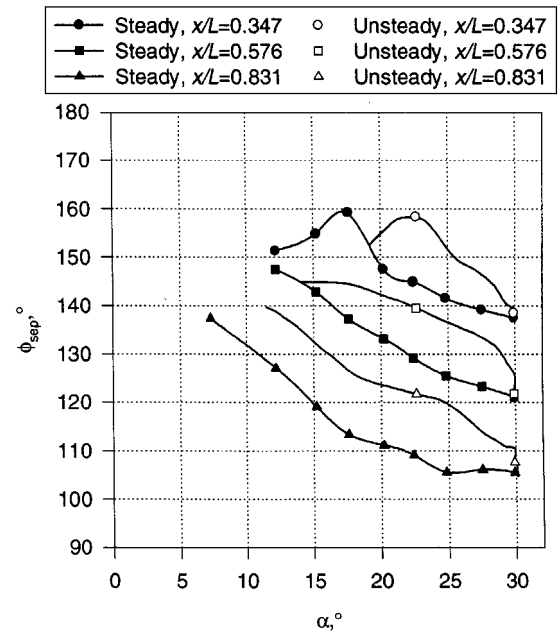

Fig. 16 Comparison of steady and pitchup maneuver (unsteady) separation location vs α for three axial locations.

the model surface and in the flowfield. Gad-el-Hak and Ho[6] also showed a delay in flow separation on the upstroke of their pitching ogive cylinder. They attributed most of the lag to moving wall effects, resulting in opposite trends on the forebody compared with the aftbody. This is consistent with the extremely high nondimensional rates they encountered ($\bar{\dot{\alpha}} = 1.05$). The much lower rates in the present experiment ($\bar{\dot{\alpha}} = 0.047$) means the unsteady flow effects will be primarily convective in nature, and so the nose and tail are affected similarly.

Montividas et al.[7] and Ericsson[18] tried to correlate lags in the flowfield with simple descriptions of the unsteady effects. They both focused on the onset of asymmetric vortex shedding at high angles of attack on ogive cylinders. Although this is a different phenomenon from crossflow separation at moderate angles of attack, both situations involve three-dimensional separation. Also, it is important to note that asymmetric vortex shedding off the prolate spheroid is not expected at the Reynolds numbers and angle-of-attack range in the data considered here. This has been experimentally verified by Goody et al.[19]

Despite the dissimilarity between ogive cylinder and prolate spheroid flowfields, the simple models suggested in Refs. 7 and 18 for the lags of the effective angle of attack use descriptions of the flow kinematics that are seemingly valid for the unsteady crossflow separation considered here. Montividas et al.[7] attempted to account for the unsteady aerodynamic effects by considering the effective angle of attack of each station on the model due to the motion of the body relative to the wind. If a model is rotating about some point x_{cg} at some rate $\dot{\alpha}$, then in addition to the velocity of the wind relative to the point of rotation, the model has a relative velocity, normal to the model axis, of $\dot{\alpha}(x - x_{cg})$. Of course, this velocity varies with position along the model axis. Combining this velocity with the relative velocity of the wind and using small angle simplifications, one can approximate an effective angle of attack as the following[7]:

$$\alpha_{\text{eff}} = \alpha - \Delta\alpha_{\text{eff}} \tag{1}$$

$$\Delta\alpha_{\text{eff}} = \dot{\alpha}\frac{x_{cg} - x}{U_\infty} \tag{2}$$

This approximation did not describe the unsteady effects in their flowfield properly.[7]

Ericsson[18] extended the idea by including convective lag effects in the flowfield. When a model changes its orientation, it takes a certain amount of time for a particle at the apex of the model to propagate this change back to a given axial location on the model. Ericsson was analyzing pointed ogive cylinders, but a similar argument can be used for the prolate spheroid if one considers that the stagnation point, which is always near the nose, approximates the model apex for this argument. The time lag for a disturbance at the apex or stagnation point to convect back to some axial location x on the model is $\Delta t = x/U_\infty$. Ericsson[18] incorporated this time lag with Eq. (2) to obtain

$$\Delta\alpha_{\text{eff}} = \dot{\alpha}\frac{x_{cg} + x}{U_\infty} \tag{3}$$

Note the difference in sign on the x term in Eq. (3) compared to Eq. (2). Equation (3) did successfully approximate the lags in asymmetric vortex shedding on the pitching ogive cylinder.[18]

For the prolate spheroid maneuvers here, x_{cg} is $L/2$. For the 30-deg pitchup maneuver, where the nominal pitch rate $\dot{\alpha}$ is 90 deg/s, $\Delta\alpha_{\text{eff}}$ using Eq. (3) will range from 1.35 deg at the nose to 4.05 deg at the tail, and $\Delta\alpha_{\text{eff}}$ is independent of time or angle of attack due to the constant pitching rate. Figure 16 shows the steady and unsteady (pitchup maneuver) separation locations as a function of α. Note that in Fig. 16 the symbols on the unsteady curves are used to differentiate the plot lines and are not an indication of the number of points in that series. Each unsteady curve includes over 100 data points. Figure 16 can be used to estimate $\Delta\alpha_{\text{eff}}$ at each instant in time by computing the horizontal distance between corresponding steady and unsteady curves. It is evident that $\Delta\alpha_{\text{eff}}$ for this flow is much larger than estimated by Eq. (3). Figure 17 shows the measured $\Delta\alpha_{\text{eff}}$ for three stations. Note that $\Delta\alpha_{\text{eff}}$ has an uncertainty of ± 2 deg. The value of $\Delta\alpha_{\text{eff}}$ does increase as one moves toward the tail, consistent with Eq. (3), but the magnitudes are several times higher than indicated by Eq. (3) and vary with α (or equivalently with t'). The lags in the crossflow separation, therefore, are an even more complex function of unsteadiness in the developing boundary layer compared to asymmetric vortex shedding.

B. Differential Time Lag Model of Goman and Khrabrov[20]

Goman and Khrabrov[20] have suggested a model for general unsteady aerodynamics that utilizes a dominant flow feature, such as separation location, as an internal state variable. For example, Goman and Khrabrov have used such a model to correlate data for pitching two-dimensional airfoils and delta wings and have even partially succeeded in describing the unsteady aerodynamics of a complex fighter configuration. Forces and moments are defined as functions of this state variable using steady data. Also, steady data are used to determine how the state variable varies with angle of attack. Then a first-order differential equation is used to describe how the state variable varies for an unsteady angle-of-attack time history. The result of this model equation is the time history of the state variable for a given maneuver, which is then used to compute the unsteady aerodynamic forces and moments.

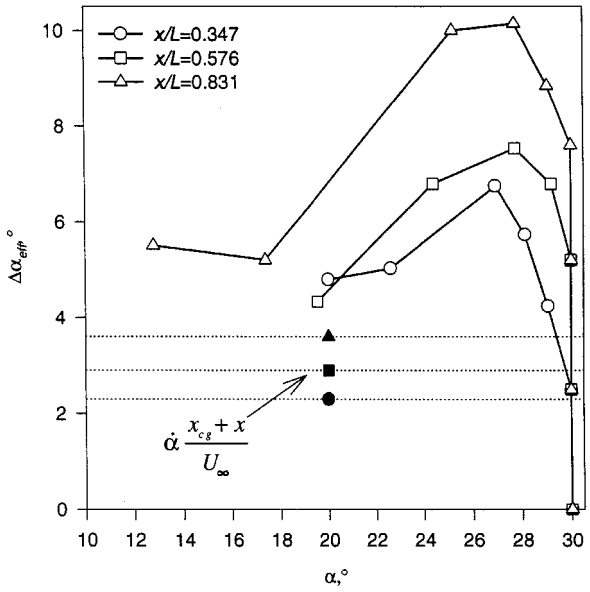

Fig. 17 Incremental effective angle of attack $\Delta\alpha_{\text{eff}}$ for the pitchup maneuver at three axial stations as a function of instantaneous angle of attack (DyPPiR pitch angle) α. Solid symbols show the effective angle of attack given by Eq. (3).

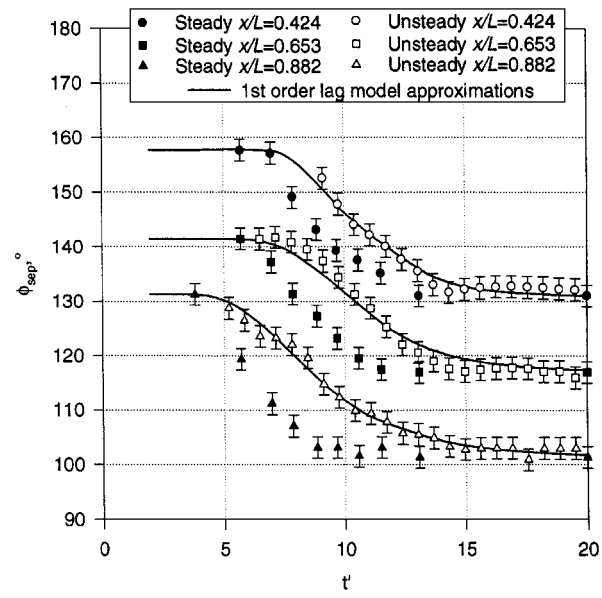

Fig. 18 First-order model fits to unsteady separation data. Solid symbols show steady (model input) data points, open symbols show unsteady separation location data points, and lines show unsteady separation location computed with model equation (5).

It is proposed to attempt to partially implement an extended version of this model on the unsteady separation data for the prolate spheroid. Goman and Khrabrov[20] always used a single or one-dimensional state-variable for their analyses. In the present case, rather than a single point of separation, there is a separation line, and there is no reason to assume that the entire line moves with a single time lag. Therefore, to extend the model of Goman and Khrabrov,[20] one can specify that the steady separation location ϕ_0 at each x/L is a function only of angle of attack:

$$\phi_0 = \phi_0(x/L; \alpha) \tag{4}$$

Given a time-varying angle of attack $\alpha(t)$, one can model the unsteady separation location at each x/L with a first-order differential equation:

$$\tau'\left(\frac{x}{L}\right)\left.\frac{\mathrm{d}\phi}{\mathrm{d}t'}\right|_{x/L} + \phi\left(\frac{x}{L}; t'\right) = \phi_0\left(\frac{x}{L}; \alpha(t')\right) \tag{5}$$

In this model equation, the first-order time lag τ' is assumed to vary over the model length. Also note that Eq. (5) has been written for nondimensional time units, and so τ' is also in nondimensional time units.

One distinction of the Goman and Khrabrov[20] model is that the time lag τ' is not determined from analysis as Montividas et al.[7] and Ericsson[18] attempted. Instead, the time lag is a parameter that is identified by fitting the model equation with experimental data. The unsteady separation data from the present prolate spheroid tests were fitted to Eq. (5) at each sensor station. Steady data were fitted with a cubic spline. One problem in fitting a first-order equation to these separation data is that a first-order equation requires an initial value for computation, but the start of separation is very difficult to identify with precision.[15] Therefore, for all cases, the first steady data point was used for the initial condition for the first-order lag computation. The prolate spheroid pitch position was used as the time-varying angle of attack $\alpha(t)$. The spline-fit input data were combined with a guessed value of τ' for each model location to compute the modeled unsteady separation location using Eq. (5). Then a root-mean-square error was computed between the modeled and measured unsteady data. Finally, the solution was iterated to find a value of τ' for each sensor that minimized the rms error. Data at sensors at $x/L = 0.194$, 0.220, and 0.271 were not used because the separation locations found by these sensors were very noisy and uncertain, most likely due to the close proximity of these three sensors to the trip posts at $x/L = 0.200$.

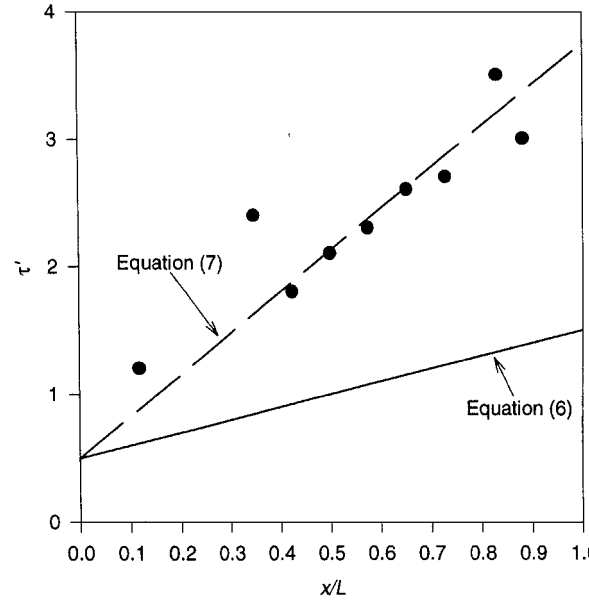

Fig. 19 Computed time lag vs model location: Symbols show values computed applying model equation (5) to the measured separation location data; Eq. (6) is shown for reference, and Eq. (7) is shown with fitted constant of $U_\infty/U_c = 3.25$, which was obtained using least-squares regression.

Figure 18 shows the modeled unsteady separation location for three x/L stations. Error bars of ± 2 deg have been added to the measured steady and unsteady data. Figure 18 shows that the first-order model of Eq. (5) does capture the time-varying nature of the unsteady separation locations reasonably, which gives hope that such a model could be combined with force and moment data in the future to yield new tools in modeling the unsteady aerodynamics of such complicated bodies.

Figure 19 plots the fitted time lags that were computed at each location. The scatter in these computed time lags reflects the uncertainty in the data, but in general it is seen that the time lag increases with x/L. This follows the qualitative trend suggested by Ericsson's model,[18] Eq. (3). This means that a significant lag in the formation of crossflow separation is the convective lag associated with the time it takes for disturbances to propagate the length of the model. However, because the lags are consistently higher than one nondimensional

time unit, either the convective velocity is much slower than the freestream velocity or there is an additional lag mechanism present.

One can compare this differential model mathematically with the algebraic models presented earlier. In both Eqs. (2) and (3), the lag in angle of attack $\Delta\alpha_{\text{eff}}$ is the product of the pitch rate $\dot{\alpha}$ and some convective time, which is essentially a time lag. Thus, for example, the effective time lag in Eq. (3), nondimensionalized in time, is

$$\tau' = (x_{\text{cg}}/L) + (x/L)$$
$$= 0.5 + (x/L) \tag{6}$$

The substitution was made that $x_{\text{cg}} = L/2$ in the present experiment. This line is plotted in Fig. 19, and the time lags of Eq. (6) fall significantly lower than those indicated from the differential model fitted to the data. This is similar to the observation presented in Fig. 17.

When Ericsson[18] extended the model of Montividas et al.,[7] he assumed that disturbances were convected at the freestream speed. If one rederives his model using an unknown convection speed U_c and if one then computes the effective time lag as was done for Eq. (6), the following relation results:

$$\tau' = (x_{\text{cg}}/L) + (x/L)(U_\infty/U_c)$$
$$= 0.5 + (x/L)(U_\infty/U_c) \tag{7}$$

Using least-squares regression to fit Eq. (7) with the data points in Fig. 19, the ratio U_∞/U_c is found to be 3.25, or $U_c = 0.3U_\infty$. Therefore, the convective velocity that dominates the time lag in this flowfield is roughly a third of the freestream velocity.

Because the dominant flow feature here is three-dimensional crossflow separation, one could presume that disturbances that impact separation must be propagated through the boundary layer. It is clear that boundary-layer velocities must be smaller than those outside the boundary layer. In Ref. 21, it is shown that the large-scale structures in a two-dimensional turbulent boundary layer propagate with a speed roughly 14 times the friction velocity:

$$U_c \approx 14U\tau = 14\sqrt{(Cf/2)}U_\infty \tag{8}$$

It is not known how the convective velocities in a three-dimensional boundary layer compare to those from two-dimensional ones, and so for the present order-of-magnitude analysis, Eq. (8) will be used. For the current flow, the skin-friction coefficient varies on the windward side from roughly 0.002 to 0.010, which yields convective velocities of the range $U_c = 0.4U_\infty$ to U_∞. Therefore, it is clear that the slower convection speeds in a turbulent boundary layer are slow enough, in order of magnitude, to potentially account for the unsteady lags observed, within uncertainties.

V. Conclusions

The time history of the separation location on a 6:1 prolate spheroid was measured experimentally for two time-dependent maneuvers. All tests were conducted at $Re_L = 4.2 \times 10^6$, and trip posts were located on the model at $x/L = 0.20$. Minima in wall shear from hot-film sensor measurements were used to indicate crossflow separation on the leeward side of the model. The data show definite lags in the formation and migration of the separation line for the pitchup maneuver but showed much weaker trends for the submarine maneuver due to weaker separations at the lower angles of attack. The data show that the lags in the development of the flowfield can lead to different flow topologies for an unsteady case as compared with the steady case at the same angle of attack. For example, some cases show that the unsteady flowfield exhibits only a primary separation, but the steady flowfield shows both primary and secondary separations. Also, the lag time constants have a different value at different locations on the model and at different points in time during the maneuver, indicating the complex nature of such an unsteady separation. The first-order time lag model of Goman and Khrabrov seems to fit the data reasonably well. The time lags obtained from such a model fit seem to indicate that the dominant convective speed of the lag is slower than freestream. It is shown that the slower convective velocity in the boundary layer is a plausible mechanism for these slower convective speeds.

Acknowledgments

The authors are grateful for Contracts N00014-87-K-0816, N00014-91-J-1732, and N0001495-I-0101 and for the years of encouragement and support by James A. Fein of the Office of Naval Research. We would also like to acknowledge Jon L. Fleming for his assistance in operating the dynamic plunge–pitch–roll (DyPPiR) model and the wind tunnel.‡

References

[1] Ahn, S., Choi, K. Y., and Simpson, R. L., "The Design and Development of a Dynamic Plunge–Pitch–Roll Model Mount," AIAA Paper 89-0048, Jan. 1989.

[2] Ahn, S., "An Experimental Study of Flow over a 6 to 1 Prolate Spheroid at Incidence," Ph.D. Dissertation, Aerospace Engineering Dept., Virginia Polytechnic Inst. and State Univ., Blacksburg, VA, 1992.

[3] McCroskey, W. J., "Some Current Research in Unsteady Fluid Dynamics," *Journal of Fluids Engineering*, Vol. 99, No. 1, 1977, pp. 8–39.

[4] Etkin, B., *Dynamics of Atmospheric Flight*, Wiley, New York, 1972, p. 178.

[5] Wetzel, T. G., "Unsteady Flow over a 6:1 Prolate Spheroid," Ph.D. Dissertation, Aerospace and Ocean Engineering Dept., Rept. VPI-AOE-232, Virginia Polytechnic Inst. and State Univ., Defense Technical Information Center, No. ADA3071412XSP, Alexandria, VA, April 1996.

[6] Gad-el-Hak, M., and Ho, C. M., "Unsteady Flow Around an Ogive Cylinder," *Journal of Aircraft*, Vol. 23, No. 6, 1986, pp. 520–528.

[7] Montividas, R. E., Reisenthel, P., and Nagib, H. N., "The Scaling and Control of Vortex Geometry Behind Pitching Cylinders," AIAA Paper 89-1003, March 1989.

[8] Smith, L. H., and Nunn, R. H., "Aerodynamic Characteristics of an Axisymmetric Body Undergoing a Uniform Pitching Motion," *Journal of Spacecraft and Rockets*, Vol. 13, No. 1, 1976, pp. 8–14.

[9] Panzer, E. C., Rediniotis, O. K., and Telionis, D. P., "The Hemisphere Cylinder in Dynamic Pitch-Up Motions," AIAA Paper 93-2963, 1993.

[10] Brandon, J. M., and Shah, G. H., "Unsteady Aerodynamic Characteristics of a Fighter Model Undergoing Large-Amplitude Pitching Motions at High Angles of Attack," AIAA Paper 90-0309, Jan. 1990.

[11] Choi, K., and Simpson, R. L., "Some Mean Velocity, Turbulence, and Unsteadiness Characteristics of the VPI&SU Stability Wind Tunnel," Aerospace and Ocean Engineering Dept., Rept. VPI-AOE-161, Virginia Polytechnic Inst. and State Univ., Blacksburg, VA, Dec. 1987.

[12] Willett, K., "Design, Development, and Implementation of a Low Cost Slotted Wall Test Section and Race Car Model for Use in Dynamic Wind Tunnel Testing," M.S. Thesis, Aerospace and Ocean Engineering Dept., Rept. VPI-AOE-259, Virginia Polytechnic Inst. and State Univ., Blacksburg, VA (in progress).

[13] Simpson, R. L., Walker, D. A., and Shinpaugh, K. A., "Description of a 1000 Sensor Constant Current Anemometer System for Locating Three-Dimensional Turbulent Boundary Layer Separations," Aerospace and Ocean Engineering Dept., Rept. VPI-AOE-185, Virginia Polytechnic Inst. and State Univ., Defense Technical Information Center, No. ADA2508273XSP, Alexandria, VA, Dec. 1992.

[14] Bellhouse, B. J., and Schultz, D. L., "Determination of Mean and Dynamic Skin Friction Separation and Transition in Low-Speed Flow with a Thin-Film Heated Element," *Journal of Fluid Mechanics*, Vol. 24, Pt. 2, 1966, pp. 379–400.

[15] Wetzel, T. G., Simpson, R. L., and Chesnakas, C. J., "Measurement of Three-Dimensional Crossflow Separation," *AIAA Journal*, Vol. 36, No. 4, 1998, pp. 557–564.

[16] Miller, J. A., "A Simple Linearized Hot-Wire Anemometer," *Journal of Fluids Engineering*, Ser. 1, Vol. 98, No. 3, 1976, pp. 550–557.

[17] Chesnakas, C. J., and Simpson, R. L., "Detailed Investigation of the Three-Dimensional Separation About a Prolate Spheroid," *AIAA Journal*, Vol. 35, No. 6, 1997, pp. 990–999.

[18] Ericsson, L. E., "Unsteady Flows," *Tactical Missile Aerodynamics: General Topics*, edited by M. J. Hemsch, Vol. 141, Progress in Astronautics and Aeronautics, AIAA, Washington, DC, 1992, pp. 490–493.

[19] Goody, M., Simpson, R. L., Engel, M., Chesnakas, C. J., and Devenport, W. J., "Mean Velocity and Pressure and Velocity Spectral Measurements Within a Separated Flow Around a Prolate Spheroid at Incidence," AIAA Paper 98-0630, Jan. 1998.

[20] Goman, M., and Khrabrov, A., "State-Space Representation of Aerodynamic Characteristics of an Aircraft at High Angles of Attack," *Journal of Aircraft*, Vol. 31, No. 5, 1994, pp. 1109–1115.

[21] Simpson, R. L., Strickland, J. H., and Barr, P. W., "Features of a Separating Turbulent Boundary Layer in the Vicinity of Separation," *Journal of Fluid Mechanics*, Vol. 79, 1977, pp. 553–594.

F. W. Chambers
Associate Editor

‡The full data set from which this paper was derived is available on the Internet at http://www.aoe.vt.edu/aoe/physical/dyppir/index.html.